Monthly Notices of the ROYAL ASTRONOMICAL SOCIETY

MNRAS **500,** 3425–3437 (2021) doi:10.1093/mnras/staa3467
Advance Access publication 2020 November 10

Systematic velocity drifts of methanol masers associated with G9.62+0.20E

G. C. MacLeod,[1,2★] J. O. Chibueze,[3,4★] A. Sanna,[5,6] J. D. Paulsen,[7] M. Houde,[1] S. P. van den Heever[2★] and S. Goedhart[8]

[1]*The University of Western Ontario, 1151 Richmond Street. London, ON N6A 3K7, Canada*
[2]*Hartebeesthoek Radio Astronomy Observatory, PO Box 443, Krugersdorp 1741, South Africa*
[3]*Centre for Space Research, North-West University, Potchefstroom 2520, South Africa*
[4]*Department of Physics and Astronomy, Faculty of Physical Sciences, University of Nigeria, Carver Building, 1 University Road, Nsukka, 410001, Nigeria*
[5]*INAF, Instituto di Radioastronomia & Italian ALMA Regional Centre, Via P. Gobetti 101, I-40129 Bologna, Italy*
[6]*INAF, Osservatorio Astronomico di Cagliari, via della Scienza 5, I-09047 Selargius (CA), Italy*
[7]*Trinity House High School, 1 Falls Rd, Little Falls, Roodepoort, 1724, South Africa*
[8]*South African Radio Astronomy Observatory, The Park, Park Road, Pinelands, 2 Fir Street, Black River Park, Observatory 7925, South Africa*

Accepted 2020 November 3. Received 2020 October 30; in original form 2020 August 27

ABSTRACT

The source G9.62+0.20E surprises again! Several of the associated 6.7- and 12.2-GHz methanol masers are experiencing contemporaneous and systematic velocity drifts. Both 6.7- and 12.2-GHz methanol features blueward of $v = +1.2$ km s^{-1} are blue shifting while those redward are red shifting. A best-fitting rotating Keplerian disc with a central mass of $\sim$12 M$_\odot$, radii $R_{\rm inner} = 5$ au and $R_{\rm outer} = 5000$ au, and at an inclination angle of 22° either precessing and/or experiencing infall explains these systematic velocity drifts. Also three more distinct 6.7-GHz methanol maser features are found to vary periodically; two very weak and one obviously periodic only after 2003. Evidence of periodicity is seen as early as 1992. Time lags are confirmed but the cause is unclear. It is possible this source will surprise again.

Key words: masers – stars: formation – stars: protostars – ISM: individual objects: G9.62+0.20E – ISM: molecules – radio lines: ISM.

1 INTRODUCTION

The monitoring of masers and, in particular, those associated with high-mass star-forming regions (HMSFRs) began almost from the moment they were first discovered (Weaver, Dieter & Williams 1968, and references therein). MacLeod & Gaylard (1996) presented long-term monitoring of methanol (CH_3OH) and hydroxyl (OH) masers and reported time lags during flares of the methanol masers. Up to 20 yr of water maser monitoring was shown in Felli et al. (2007); most of these were highly variable in both flux density and velocity. Goedhart, Gaylard & van der Walt (2003) discovered periodicity in the class II methanol masers associated with G9.62+0.20E and there are presently 25 known periodic maser sources (Goedhart, Gaylard & van der Walt 2004; Goedhart et al. 2009; Araya et al. 2010; Szymczak et al. 2011; Fujisawa et al. 2014; Maswanganye et al. 2015, 2016; Sugiyama et al. 2015; Szymczak, Wolak & Bartkiewicz 2015; Szymczak et al. 2016, 2018b; Sugiyama et al. 2017; Proven-Adzri et al. 2019; Olech et al. 2020). Some even have contemporaneous periodic variations in transitions of other molecules, for example, hydroxyl (Goedhart et al. 2004; Green et al. 2012; Olech et al. 2020), formaldehyde (Araya et al. 2010), and water (Szymczak et al. 2016; Olech et al. 2020). The periodic maser source, G323.46−0.08, underwent a significant flaring event (Proven-Adzri et al. 2019) similar to those resulting from proposed accretion events (Moscadelli et al. 2017; MacLeod et al. 2018); it is not known if it was periodic before the flare. The cause of maser periodicity remains an open question, the competing proposed explanations are a pulsating protostellar object (Inayoshi et al. 2013; Sugiyama et al. 2015), periodic accretion (Araya et al. 2010), a rotating spiral shock (Parfenov & Sobolev 2014), or a colliding wind binary (CWB) system (van der Walt et al. 2016; van den Heever et al. 2019, and references therein).

Similar to the water masers where velocity variations are detected (Felli et al. 2007), various authors present results of velocity variations in methanol maser features. Szymczak et al. (2018a) measured velocity drifts in methanol features in four HMSFRs. They proposed this drift could be explained by deferentially varying line blended masers in a feature. However, they did suggest that for some the drift may be the result of an infalling motion.

Specifically, G9.62+0.20E is an HMSFR with a hypercompact H II region (Garay et al. 1993) and with various maser species projected against it (Sanna et al. 2015; Sugiyama et al. 2015). It was shown that the 6.7-, 12.2-, and 107-GHz methanol transitions flare simultaneously and are periodic (van der Walt, Goedhart & Gaylard 2009). The best-fitting period of this prototypical periodic methanol maser is 243.3 d (Goedhart et al. 2014). Goedhart et al. (2019) presented periodic flaring of the hydroxyl masers associated with G9.62+0.20E. The parallax distance of G9.62+0.20E is 5.2 ± 0.6 kpc from the Sun (Sanna et al. 2009).

In this paper, we present the results of long-term monitoring using the Hartebeesthoek Radio Astronomy Observatory (HartRAO) of masers associated with G9.62+0.20E at 6.7- and 12.2-GHz methanol

★ E-mail: gord@hartrao.ac.za (GCM); james.chibueze@gmail.com (JOC); fanie@hartrao.ac.za (SPVDH)

Table 1. Spectral transitions observed, monitoring start month, and receiver packages used at HartRAO.

Mol.	Receiver	Maser		Beam	Band	Velocity		Sensitivity	Monitoring
		Transition	Frequency	width	width[a]	Range	Resolution	3σ rms	start
	(cm)		(GHz)	(arcmin)	(MHz)	(km s^{-1})	(km s^{-1})	(Jy)	Month
CH_3OH	4.5	$J = 5_1 \rightarrow 6_0\ A^+$	6.668 518	7.0	0.64[b]	14.5	0.112	1.0–1.5	1999 Feb
					1.0	22.5	0.044	0.8–1.2	2003 Mar
	2.5	$J = 2_0 \rightarrow 3_{-1}\ E$	12.178 593[c]	4.0	0.64[b]	7.75	0.061	1.5–2.5	2000 Jan
					2.0	24.5	0.048	0.6–0.9	2003 Mar

[a]A dual polarization, 1024 channel each, spectrometer was employed after 2003 March 27.
[b]A single polarization, 256 channel, spectrometer at LCP was employed until 2003 March 27.
[c]The receiver was offline from 2016 January 1 to August 9.

transitions. We develop simplified methods to analyse the data in dynamic spectra. We report the detection of new periodic methanol maser features and investigate velocity variations.

2 OBSERVATIONS

The observations reported here were made using the 26-m telescope of Hartebeesthoek Radio Astronomy Observatory (HartRAO).[1] Both the 6.7-GHz (4.5 cm) and 12.2-GHz (2.5 cm) receivers are dual, left (LCP) and right (RCP), circularly polarized receivers but the former is an ambient temperature receiver while the latter is cryogenically cooled. The two polarizations of each receiver are calibrated independently relative to Hydra A and 3C 123, assuming the flux scale of Ott et al. (1994). For observations taken after 2010 December 16 the point-source sensitivity (PSS) from calibration testing for the 6.7-GHz receiver is 5.58 and 4.49 Jy K^{-1} for LCP and RCP, respectively. For the 12.2-GHz receiver, the PSS values used are 7.81 (LCP) and 7.28 Jy K^{-1} (RCP). The PSS values changed over time owing to changes to each receiver system. Values prior to 2008 October 01 were taken from Goedhart et al. (2003, 2014). Position checks are completed for all observations: pointing correction factors determined for the 6.7- and 12.2-GHz observations are less than 10 per cent. For the 6.7- and 12.2-GHz observations the beamsizes were 7 and 4 arcmin, respectively. For more information of each receiver set-up and spectrometer during the course of the long-term monitoring (see MacLeod et al. 2018). In Table 1, we present information for each transition observed and typical sensitivities obtained.

Monitoring observation start months are given in Table 1. Observations were made every 10 to 15 d in each transition, but the cadence of observations varied depending on the availability of the telescope, and the weather conditions. At times observations were done daily, but there are also observations separated by weeks. No spectroscopic observations were taken between 2003 April and August resulting from a failure of the 256 channel spectrometer and between 2008 September and 2010 December when the 26-m antenna underwent repairs (Gaylard 2010). During the first break in observations both the spectrometer was upgraded to 1024 channels, the intermediate frequency was increased from 60 to 160 MHz, and the local standard of rest (LSR) velocity correction software was modified. The result of this was improved velocity resolution and sensitivity but a slight a velocity discontinuity in both transitions, about 0.05 km s^{-1}, is noticeable. This discontinuity is the result of slight differences in the calculations in the LSR velocity correction. The 12.2-GHz CH_3OH receiver was offline for repairs between 2016 January 10 and August 9. The coordinates of G9.62+0.20E adopted in our observations are RA = 18^h 06^m 14^s.8 and Dec. = −20° 31′ 32″.1 (J2000).

[1]See http://www.hartrao.ac.za/spectra/ for further information.

3 DATA ANALYSIS

The genesis of this work was the production of dynamic spectra. Each dynamic spectra is the compilation of individual spectra, examples plotted in Fig. 1, taken in a particular spectral line transition and plotted as a contour plot with Modified Julian Date (MJD, x-axis), LSR velocity ($v_{\rm LSR}$, y-axis), and flux density (contours). Dynamic spectra are a powerful way to present long-term monitoring. Interpreting such plots can be daunting considering they contain a great deal of information. Plotting a horizontal cut through them, along a single velocity channel, produces a typical time-series plot such as those seen here in Fig. 4. Adding the time-series of sequential channels produces a time-series of integrated flux density, see Fig. 7. Likewise, average spectra are produced by adding vertical cuts, individual epochs of observation, together. For example, this is particularly powerful when describing the spectral shape during a maximum in the flare cycle.

Most methanol masers are relatively stable over months to years and as a result, features identified in the spectra are visible across dynamic spectra likened to vapour trails, or contrails, produced by airplanes across the sky. The dynamic spectra at 6.7 (Fig. 2) and 12.2 GHz (Fig. 3) here for G9.62+0.20E are comprised of 973 and 879 spectra, respectively. Each represent consecutive epochs of observation between 1999 February and 2000 January to 2020 September for 6.7- and 12.2-GHz methanol transitions, respectively. We develop simplified analysis processes to extract the main spectral properties from these dynamic spectra. In particular, we determine the (1) general trend of maser flux density over time (see Fig. 4), (2) period of the flaring phenomenon (see Fig. 4), (3) time lags between when various masers reach their respective maxima (see Fig. 11), and (4) variations of maser velocities (velocity drifts, see Fig. 8).

For clarity, a specific velocity channel of the 512 channels or 256 for the pre-2003 observations, that comprise each spectrum at each transition are referred to as 'channel' or 'chan', $v_{\rm chan_v}$; its associated flux density is referred to as $F_{\rm chan_v}$. When the term 'feature' in a particular spectra is written it refers to a group of sequential channels that appear to be distinguishable emission; these features may be comprised of one or more masers (components) but line blended. However, there is no spatial information in spectra and a feature here does not refer to a specific maser 'cloudlet' – a distinct gas condensation, or centre of emission, on a spatial image (e.g. Sanna et al. 2017). At all times every velocity representation is an LSR velocity, $v_{\rm LSR}$, regardless the subscript unless otherwise stated.

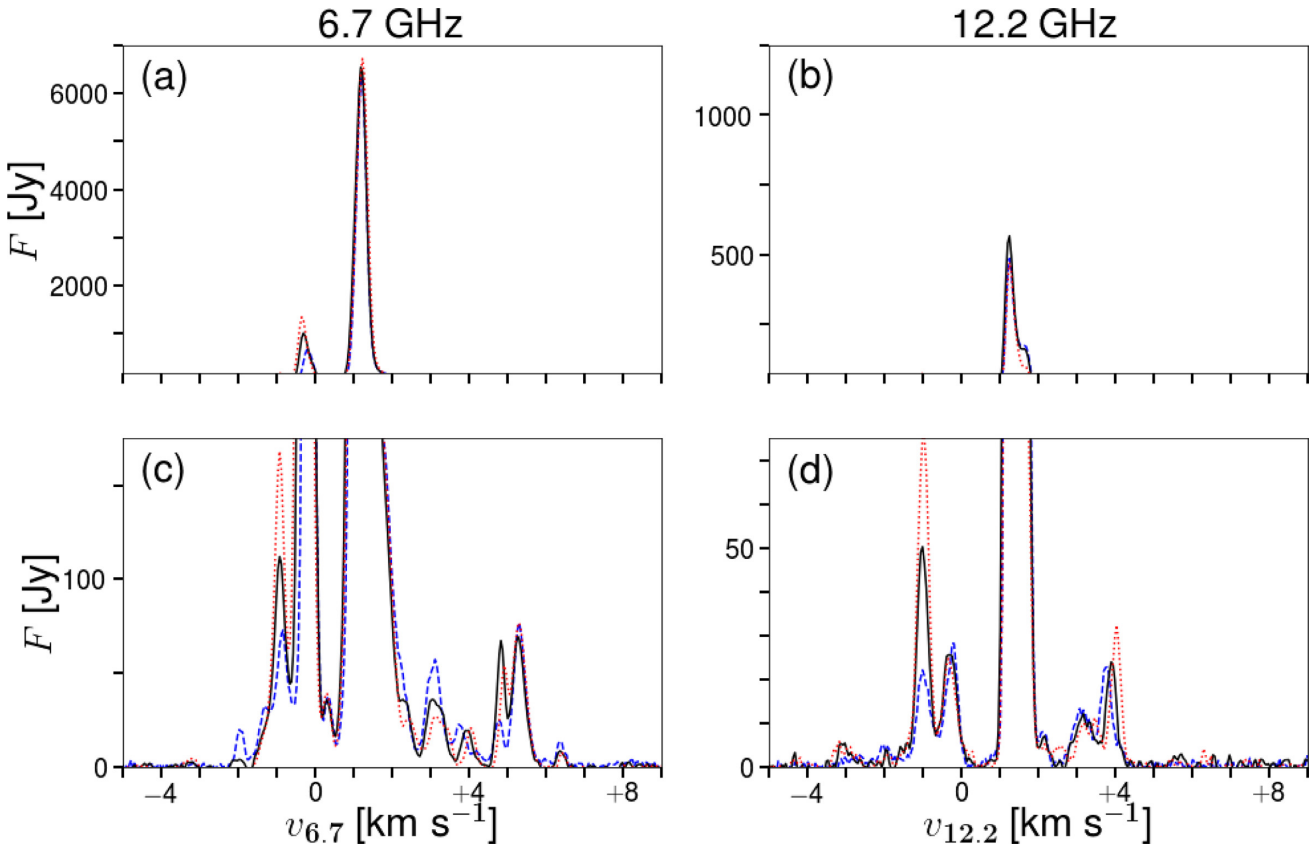

Figure 1. Individual spectra are plotted for both 6.7- (a, c) and 12.2-GHz (b, d) methanol masers taken during the maximum of FC_{10} (dashed blue lines), FC_{20} (solid black lines), and FC_{30} (dotted red lines). Spectra of 6.7-GHz methanol masers taken on 2005 February 28, 2011 October 28, and 2018 June 23 are plotted. Spectra of 12.2-GHz methanol masers taken on 2005 February 28, 2011 October 29, and 2018 July 1 are plotted.

3.1 Creating time-series

A simple process is used to study the variability of individual features both in flux density and velocity in these dynamic spectra. The central v_{chan_ν} of a given feature is selected from unambiguous peaks in the spectra, or in the dynamic spectra. For each v_{chan_ν} selected a time-series is created comprised of F_{chan_ν} verses MJD. Around each central v_{chan_ν}, a velocity range, anywhere from ± 0.5 to 1.0 km s^{-1}, is set, preferably larger than the velocity extent of the feature. This extent varied for each feature dependent upon its isolation in the spectra from other features. Then in each epoch the maximum flux density, and corresponding velocity, is selected. This maximum flux density is referred to as the corrected (for velocity variation) flux density F_{C_ν} ($\geq F_{\mathrm{chan}_\nu}$) and the velocity the corrected velocity v_{C_ν}. At the same time the integrated flux density, F_{Int_ν}, is found across each velocity extent. Ergo four time-series over the total MJD range are produced, they are (1) the flux density in a single channel (v_{chan_ν}), (2) F_{C_ν}, (3) F_{Int_ν}, and (4) v_{C_ν}. For (1) through (3) the trending variations and periodic nature of each feature is studied; for (4) velocity drifts are. It was impossible to differentiate between the more heavily line-blended features especially in the velocity extent $v_{chan_\nu} = 1.2 \pm 0.5$ km s^{-1} for both methanol transitions.

3.2 Peak-to-peak (PP) periodicity measurements

Goedhart et al. (2014) stated the period for the methanol masers in G9.62+0.20E is $\tau_{G14} = 243.3 \pm 2.1$ d. It was determined from analysing several features over thirteen flare cycles. Each flare cycle is referred to as FC_n where n signifies which flare cycle it is; in the presented data set n = 1–33. The maxima, or phase zero of FC_n, for time-series plots associated with G9.62+0.20E are used because this phase of the flare is easily identifiable in the temporal profile. The brightest 6.7-GHz maser feature $v_{6.7}$ =1.2 km s^{-1} reached a maximum on 1999 February 26 (MJD 51235), hereafter this is referred to as D_{G14}, during the first flare cycle, referred to as FC_1. With this the ephemeris is

$$D_{G14_n} = (243.3 \pm 2.1) \times (n - 1) + (51235 \pm 16). \quad (1)$$

The error, 16 d, is the average of the date difference with observations before and after D_{G14_1}. Its accuracy in predicting future flares is limited primarily by the error on period; it is multiplicative ($= n \times$ 2.1 d). The error on D_{G14_1} is only ∼7 per cent of τ_{G14} and is additive.

The $v_{6.7}$ and $v_{12.2}$ =1.2 km s^{-1} single-dish features are a blend of multiple bright maser spots residing in a small area (∼35 au) Sanna et al. (2015). Ergo time lags between these maser spots are expected to be small and the date represents an average of them.

Of the 33 flare cycles since 1999 almost all, 30 (FC_{16}–FC_{18} missing) and 27 (FC_1, FC_2, FC_{16}–FC_{18}, and FC_{27} missing) for the 6.7- and 12.2-GHz CH_3OH masers, respectively, have been monitored. These are large enough samples to apply a statistical analysis to, and obtain accurate periodicities (τ) and potential time lags (*Tl*).

The periodicity of maser features is determined as follows. The dates of successive maxima are projected from D_{G14} assuming the period is τ_{G14}. These flare cycles are enumerated and referred to as FC_n for n = 1–33. Then a temporal window in which a search is made is set at ±25 per cent of the assumed period, or ±60 d, and

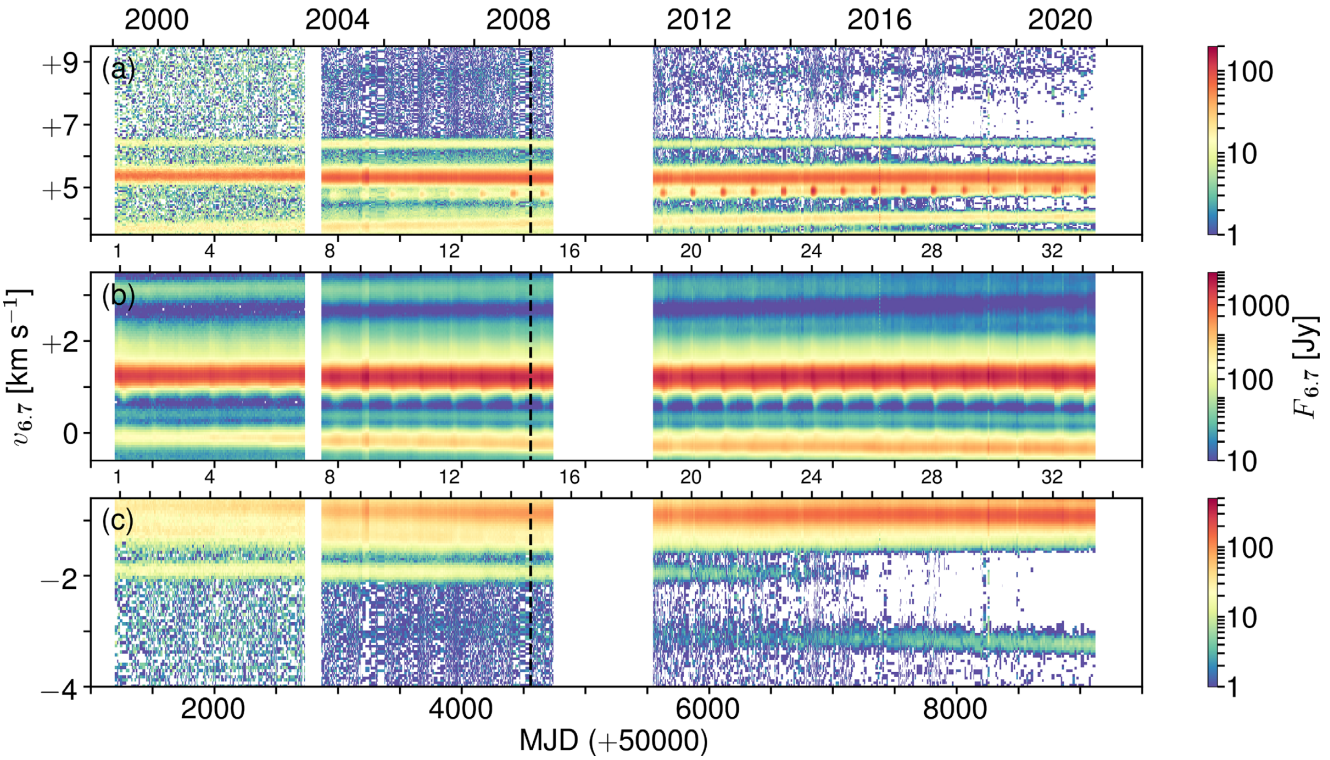

Figure 2. Dynamic spectra of the 6.7-GHz methanol masers in the velocity ranges: (a) $v_{\mathrm{chan}_{6.7}} = +4$–$+10$ km s^{-1}, (b) $v_{\mathrm{chan}_{6.7}} = +0.5$–$+4$ km s^{-1}, and (c) $v_{\mathrm{chan}_{6.7}} = -5$–$+0.5$ km s^{-1} associated with G9.62+0.20E. The secondary axis on (b) and (c) demarcates FC$_n$ from $n = 1$–33 as determined from the ephemeris presented in equation (1) (Goedhart et al. 2014). The black dashed vertical lines demarcate the date of the Sanna et al. (2015) interferometric observations at 6.7 GHz.

centred on FC$_n$. This mitigates the risk of selecting a maximum flux density associated with either FC$_{n\pm1}$. Finally, the maximum flux density (F_{v_n}) per feature, and its corresponding MJD date D$_{v_n}$, is found in each temporal window in FC$_n$ for $n = 1$–33. The PP time-delay is determined from the difference of dates of successive maxima, $\Delta D_{v_n} = \mathrm{D}_{v_{n+1}} - \mathrm{D}_{v_n}$, and the mean of these represents the periodicity, τ_v, of the flaring feature at a given velocity and given transition (defined as v_v).

The standard deviation, 1σ, is estimated from the mean of the set of time-delays. If the standard deviation is greater than half the value of the temporal window (>30 d) then it is uncertain if this feature is periodic unless other evidence of periodicity is present, e.g. uncertain for the single v_{chan} analysis or v_{C_v} but certain for F_{Int_v} time-series. The velocity discontinuity has no effect on flux density analysis because the velocity ranges selected are much greater than it. Periodicities for a F_{C_v} and F_{Int_v} time-series are represented by τ_{C_v} and τ_{Int_v}, respectively. The Lomb–Scargle (LS) periodogram method (Scargle 1982) is employed as an independent measure of these periods.

3.3 Measuring time lags

The method above also provides a determination of time lags between features. Each feature is compared to the maxima dates of the $v_{6.7} = +1.2$ km s^{-1} feature. A time-lag is determined using Tl_{v_n}(feat)= D_{v_n}(feat)−D$_{6.7_n}$(+1.2 km s^{-1}) for each FC$_n$. The mean of these for F_{C_v} and F_{Int_v} represent the measured time lags for the feature, Tl_{C_v} and Tl_{Int_v}, respectively. The 1σ standard deviation is also estimated for the normalized distribution about the mean. If the standard deviation is larger than the mean then the time lag is not statistically significant. If $Tl < 0$, then the feature in question reaches its maximum prior to that of the feature at $v_{6.7} = +1.2$ km s^{-1}; the converse is true if $Tl > 0$.

3.4 Measuring velocity drifts

Visual inspection of the dynamic spectra is first completed to both identify periodicity and velocity drift. With regards velocity drift, this inspection will inform the determination of whether a feature is velocity drifting. The corrected flux density method above also identifies the velocity, v_{C_v}, at which the corrected flux density, F_{C_v}, is associated for each epoch of observation and selected feature. Linear regression fitting is applied to these velocity time-series. For each feature, the slope of the linear equation (M$_{C_v}$), with errors, describes the velocity drift, and the goodness of fit ($R^2_{C_v}$) are found. A low value of R$^2_{C_v}$ implies either there is no velocity drift or there is no correlation. The mean velocity of the set of v_{C_v} for a given feature and standard deviation are calculated. No effort is made to correct the velocity discontinuity. Only the higher sensitivity data with better resolution obtained after 2003 August are analysed to avoid this issue.

Finally, the veracity of the statistical analysis method of this data is tested by fitting multiple Gaussian profiles to selected epochs of observation after 2003 August. This method of fitting produces Gaussian-fitted velocities (V_{G_v}), peak flux densities (F_{G_v}), and full width at half-maximum (FWHM) line widths (W$_{G_v}$). Thereafter, linear regression fitting is employed to determine the velocity drift,

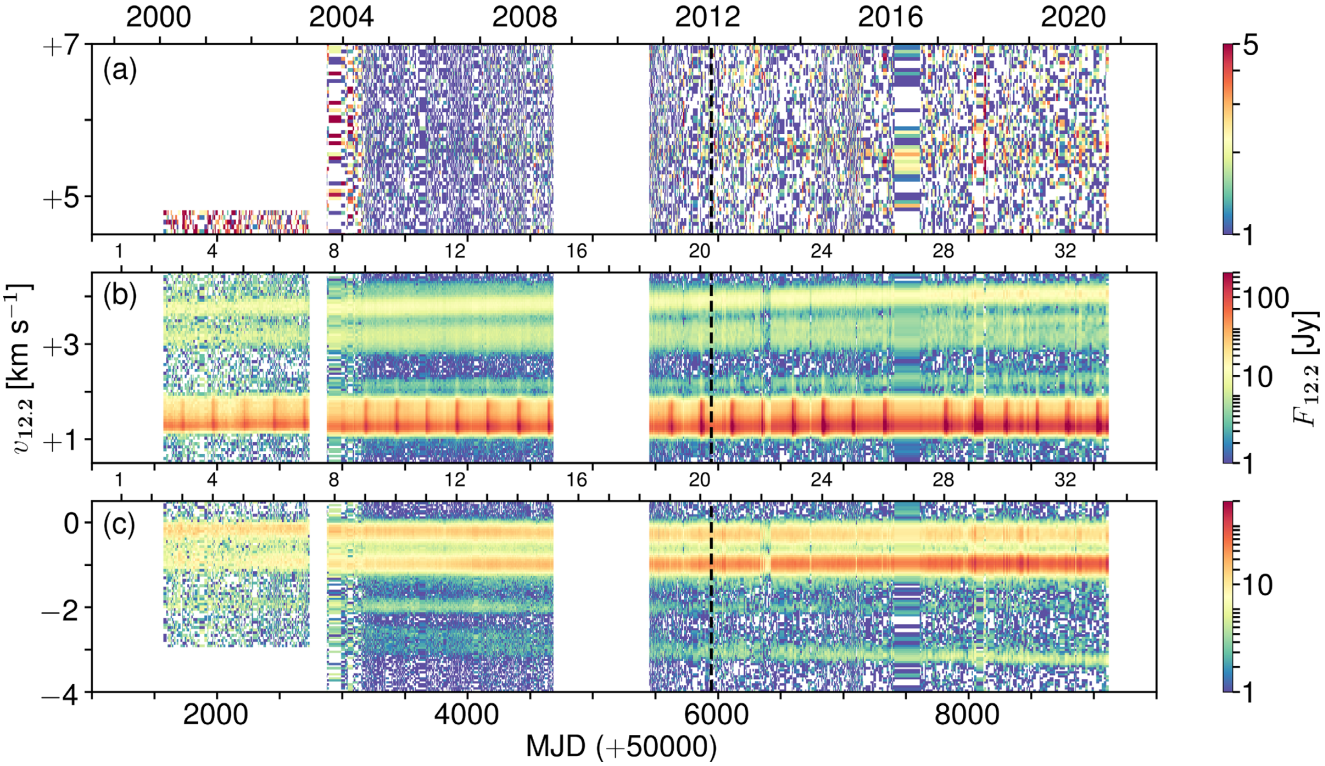

Figure 3. Dynamic spectra of the 12.2-GHz methanol masers in the velocity ranges (a) $v_{\mathrm{chan}_{12.2}} = +4$–$+10$ km s^{-1}, (b) $v_{\mathrm{chan}_{12.2}} = +0.5$–$+4$ km s^{-1}, and (c) $v_{\mathrm{chan}_{12.2}} = -5$–$+0.5$ km s^{-1} associated with G9.62+0.20E. The secondary axis on (b) and (c) demarcates FC$_n$ from $n = 1$–33 as determined from the ephemeris presented in equation (1) (Goedhart et al. 2014). The black dashed vertical lines demarcate the date of the Sanna et al. (2015) interferometric observations at 12.2 GHz.

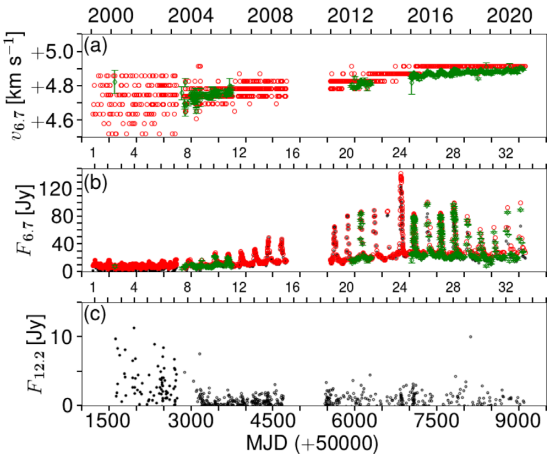

Figure 4. Time-series plots for (a) $v_{C_{6.7}}$ (red circles) and $v_{G_{6.7}}$ (green diamonds with error bars), (b) $F_{C_{6.7}}$ (red circles), $F_{G_{6.7}}$ (green diamonds with error bars) and $F_{6.7}(v_{\mathrm{chan}} = +4.8\,\mathrm{km\,s^{-1}})$ (black circles), and (c) $F_{12.2}(v_{\mathrm{chan}} = +4.8\,\mathrm{km\,s^{-1}})$ (black circles).

M_{G_v} and goodness of fit $R^2_{G_v}$. The mean velocity of the Gaussian-fitted velocities and 1σ standard deviation are determined.

4 RESULTS

Individual spectra from the maximum in FC$_{10}$ (2005 February 28), FC$_{20}$ (2011 October 28), and FC$_{30}$ (2018 June 23) for the 6.7-GHz methanol masers are shown in Fig. 1. Similarly, the corresponding spectra of 12.2-GHz methanol masers taken on 2005 February 28, 2011 October 29, and 2018 July 1 are plotted in Fig. 1. In order to see the richness of the spectra for each transition, the graphs are divided into contiguous plots, e.g. for 6.7 GHz $0 \leq F_{6.7} \leq 175$ Jy in the lower panel (c) and $175 \leq F_{6.7} \leq 7000$ Jy in the upper panel (a). In Fig. 2, the dynamic spectra of the monitoring results of the 6.7-GHz methanol masers associated with G9.62+0.20E are presented. In this image, there are three contiguous velocity ranges in order to improve the visibility of features. Likewise, the 12.2-GHz methanol masers dynamic spectra are plotted in Fig. 3 and again broken into three velocity ranges. In both figures, the dates of interferometric observations discussed in Sanna et al. (2015) are demarcated. The ephemeris described in equation (1) (FC$_n$ for n = 1–33) is shown on the upper axes of (b) and (c) in both plots for easy referencing. Contrails of features are evident in both transitions, even for pre-2003 observations where the sensitivity and velocity extent was lower than after. In each, we can see several features strengthening while others are weakening. Three new 6.7-GHz methanol features, $v_{6.7} \sim -3.0$, $+4.8$, and $+8.0$ km s^{-1}, are detected after 2002 in Fig. 2; the $v_{6.7} \sim -2.0$ km s^{-1} is no longer detectable after 2015. Features at $v_{12.2} \sim +2.0$ and -3.0 km s^{-1} have activated while that at $v_{12.2} \sim -2.0$ km s^{-1} is weakening. The flux density for features at $v \sim -2.0$ and -3.0 km s^{-1} in both transitions are trending together, the former weakening, the latter strengthening. The velocity discontinuity mentioned above is visible in each dynamic spectra.

4.1 Periodicity results

In Fig. 2, the most pronounced periodic flaring nature is evident at $v_{6.7} = +1.2$ km s^{-1}. Periodic flaring is also evident in other features between -1.0 and $+5.0$ km s^{-1}, in the 6.7-GHz methanol maser

Table 2. PP periodicity analysis of time-series for F_C and F_{Int} for features in the 6.7- and 12.2-GHz methanol dynamic spectra. The velocity quoted is the mean of the corrected velocities. The total velocity extent, over which flux density is integrated, is given as $v_{Int}(\Delta v)$ and read as $v_{Int} \pm \Delta v$. Otherwise errors, presented in parenthesis, are measures of 1σ standard deviation and applied to the last decimal place. The mean time lag for each feature of Tl_{Int} ($=D_{Int}(feat) - D_{Int}(+1.2\,km\,s^{-1})$) is given.

Trans.	Corrected flux density			Integrated flux density			Var.[a]	Tl_{Int}	Comments
	v_C	F_C^b	τ_C^c	v_{Int}	F_{Int}^d	τ_{Int}^c			
(GHz)	(km s^{-1})	(Jy)	(d)	(km s^{-1})	(Jy km s^{-1})	(d)		(d)(1σ)	
6.7	+8.2(2)	16	245(28)	+8.30(0.66)	2.1	242(13)	*p*	+11(13)	Complex[f]
6.7	+8.6(2)[e]			+8.65(0.26)	1.5	241(24)	*p*		New
6.7	+8.3(1)[e]			+8.32(0.02)	0.2	244(32)	*n*		
6.7	+8.0(1)[e]			+8.01(0.24)	1.5	244(10)	*p*		New
12.2	+8.3(2)	20	241(48)	+8.22(0.34)	1.0	243(47)	*n*	+30(50)	
6.7	+6.39(3)	26	237(59)	+6.54(0.44)	5.2	234(51)	*n*	+2(34)	
6.7	+5.29(2)	112	250(43)	+5.49(0.40)	42.0	240(40)	*n*	+26(32)	
12.2	+5.6(3)	22	251(51)	+5.51(0.60)	3.2	243(43)	*n*	+9(48)	
6.7	+4.82(7)	143	244(6)	+4.72(0.20)	26.5	244(6)	*p*	−4(12)	New
6.7	+3.9(1)	30	238(42)	+3.88(0.37)	11.4	240(36)	*n*	−12(21)	
12.2	+3.9(1)	51	240(28)	+3.89(0.43)	18.1	244(38)	*n*	+9(31)	
6.7	+3.14(4)	76	243(29)	+3.05(0.42)	34.5	242(29)	*p*	0(17)	
12.2	+3.16(7)	21	243(23)	+2.84(0.34)	7.3	243(23)	*p*	+20(45)	Complex[f]
6.7	+2.31(5)	61	242(17)	+2.48(0.24)	13.2	242(17)	*p*	−3(6)	Complex[f]
12.2	+2.16(8)	20	242(10)	+2.26(0.29)	6.2	242(10)	*p*	+11(43)	
6.7	+1.78[g]	239	242(21)[e]	+1.80(0.13)	60.5	241(20)	*p*	−3(6)	Complex[f]
12.2	+1.78[g]	403	243(7)[e]	+1.78(0.14)	20.6	243(7)	*p*	0(1)	Complex[f]
6.7	+1.21(2)	8642	243(18)	+1.23(0.18)	2377.5	243(18)	*p*	–	Complex[f]
12.2	+1.250(3)	1366	242(7)	+1.25(0.19)	387.6	242(7)	*p*	−1(22)	Complex[f]
6.7	+0.72[g]	138	244(9)	+0.72(0.20)	154.8	245(9)	*p*	−14(13)	Complex[f]
12.2	+0.72[g]	5	243(32)	+0.72(0.19)	3.5	243(13)	*p*	+10(43)	
6.7	+0.33(6)	63	244(27)	+0.39(0.22)	18.2	245(23)	*p*	−19(8)	New?
6.7	−0.27(6)	1820	242(22)	−0.31(0.22)	487.8	243(27)	*p*	−13(12)	
12.2	−0.26(5)	43	239(42)	−0.31(0.31)	16.9	239(42)	*n*	+9(30)	
6.7	−0.90(3)	233	246(33)	−0.92(0.31)	86.4	246(34)	*n*	−21(22)	Complex[f]
12.2	−1.01(2)	127	240(46)	−1.11(0.34)	43.9	238(29)	*n*	+8(33)	
6.7	−1.18(6)	74	240(49)	−1.39(0.24)	15.2	238(37)	*n*	+24(20)	Complex[f]
6.7	−1.95(5)	30	243(38)	−1.96(0.15)	5.0	232(41)	*n*	+29(32)	
12.2	−2.0(1)	28	240(31)	−2.04(0.26)	4.1	240(31)	*n*	+35(44)	
6.7	−3.1(2)	16	244(39)	−3.01(0.50)	4.6	238(57)	*n*	−6(42)	
12.2	−3.0(3)	32	240(46)	−3.89(1.30)	8.1	240(47)	*n*	−4(30)	Complex[f]
$Ave_{6.7}$			243(1)			243(2)			
$Ave_{12.2}$			242(1)			242(1)			
Ave_{all}			242(1)			242(2)			

[a]Periodic flaring: yes (*p*), no (*n*), or uncertain (*u*).
[b]Peak corrected flux density during monitoring period.
[c]Period from the average of the differences of PP flux densities.
[d]Peak integrated flux density during monitoring period.
[e]Determined periodicity of the red-, neutral, and blue-shifted components of +8.2 km s^{-1} separately.
[f]Complex implies visual inspection identifies line blending and/or multiple features present.
[g]Used v_{chan_v} rather than v_{C_v}.

emission. Likewise, periodic 12.2-GHz methanol maser emission is also present in Fig. 3 between $v_{12.2} = +1.0$ to $+2.5$ km s^{-1}. All features identified in these dynamic spectra are analysed using the simple periodicity method described above. Both the corrected flux density (F_{C_v} and integrated flux density (F_{Int_v}) time-series per feature are processed using the PP periodicity method described above and presented in Table 2. A similar analysis was done for the flux density at v_{chan_v} but not shown; the F_{chan_v} results were less reliable (larger errors). We identify nine (possibly four new) 6.7 GHz and five 12.2-GHz methanol periodic maser features. The maser emission at $v = +0.75$ km s^{-1} for both 6.7 and 12.2 GHz are periodic but it is unclear if these are independent of the flaring of the brightest feature at $v = +1.2$ km s^{-1}. There are also striations across the velocity extent present in Fig. 2. These coincide with maxima in each FC_n and are not artefacts of observation nor the construction of the dynamic spectra. It is not possible to identify individual features in these striations owing to a lack of sensitivity.

The new feature at $v_{6.7} = +4.8$ km s^{-1}, presented in Fig. 4, has period of $\tau_{Int_{6.7}} = 244 \pm 6$ d. There is some evidence of weak flaring activity prior to 2003 but it is difficult to identify as periodic. It has associated weak 12.2-GHz emission, $F_{C_{12.2}} \leq 15$ Jy, in the same velocity extent. This figure includes the Gaussian-fitted results. The $F_{G_{6.7}}$ results follow closely those for $F_{C_{6.7}}$, $\tau_{C_{6.7}} = 244 \pm 6$ d versus $\tau_{G_{6.7}} = 245 \pm 6$ d. For both $F_{C_{6.7}}$ and $F_{G_{6.7}}$ time-series the values determined via the LS periodogram method (Scargle 1982) are the same, $\tau_{LS_{6.7}} = 243$ d. It was found that a single maser, with a line width of $w_{G_{6.7}} = 0.23 \pm 0.04$ kms, best fitted the $v_{G_{6.7}} = +4.84 \pm 0.06$ km s^{-1} maser feature.

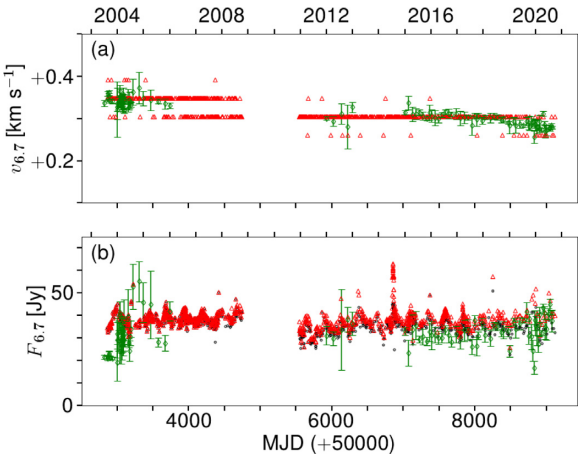

Figure 5. Time-series plots of (a) $v_{C_{6.7}}$ (red triangles) and $v_{G_{6.7}}$ (green diamonds with error bars) and (b) $F_{C_{6.7}}$ (red triangles), $F_{6.7}(v_{\rm chan} = +0.35\ {\rm km\,s^{-1}})$ (black circles) and $F_{G_{6.7}}$ (green diamonds).

A second possibly periodic feature at $v_{6.7} = +0.33\ {\rm km\,s^{-1}}$ ($\tau_{{\rm Int}_{6.7}} = 245 \pm 23$ d) was previously detected but not reported as periodic (Goedhart et al. 2014). It is visibly periodic in the dynamic spectra even in 1999. A time-series plot of this feature is shown in Fig. 5. It is possible the periodic masers that brace it, at $v_{6.7} = -0.27$ and $+1.2\ {\rm km\,s^{-1}}$, affect this feature. As they flare their long Gaussian tails rise creating the appearance of periodicity in this feature. Included in Fig. 5 are the Gaussian-fitted results ($F_{G_{6.7}}$). Some flaring is present in this fitted data. An estimate of a possible period is made difficult by too few epochs with fitted Gaussians, the value estimated, $\tau_{G_{6.7}} = 237 \pm 50$ d, suggests no periodicity. No periodicity was found via the LS method either. Very weak or no 12.2-GHz methanol maser emission is detectable towards it. It is not clear if this is a periodic feature.

A very weak 6.7-GHz methanol maser feature at $v_{6.7} \sim +8.2\ {\rm km\,s^{-1}}$ appears to be periodic in Fig. 2. It is sufficiently isolated from other features such that it cannot be influenced by them. Visual inspection of this dynamic spectra suggests it is two features, at $v_{6.7} \sim +8.0$ and $+8.6\ {\rm km\,s^{-1}}$, this is more clearly seen in Fig. 6. The 6.7-GHz interferometric observations (Sanna et al. 2015) were taken during the quiescent phase of FC_{14}, perhaps missing this feature. These are very weak features, $F_{6.7} \leq 10$ Jy, ergo their analysis is performed only for $F_{{\rm Int}_{6.7}}$. Presented are three $F_{{\rm Int}_{6.7}}$ time-series plots of the sequential velocity ranges in Fig. 7 (a) $v_{{\rm Int}_{6.7}} = +8.38$–$+8.91\ {\rm km\,s^{-1}}$ (red), (b) $v_{{\rm Int}_{6.7}} = +8.29$–$+8.34\ {\rm km\,s^{-1}}$ (black), and (c) $v_{{\rm Int}_{6.7}} = +7.77$–$+8.25\ {\rm km\,s^{-1}}$ (blue). The results shown in Table 2 indicate the $v_{{\rm Int}_{6.7}} = +8.01$ and $+8.65\ {\rm km\,s^{-1}}$ features are periodic or quasi-periodic. The 1σ standard deviations of periodicities for $v_{{\rm Int}_{6.7}} = +8.01$ and $+8.65\ {\rm km\,s^{-1}}$ were larger if only two sequential velocity extents are used. The central $F_{{\rm Int}_{6.7}}$ is not periodic and its mean value is 0.12 ± 0.04 Jy km s^{-1}, suggestive $v_{{\rm Int}_{6.7}} = +8.01$ and $+8.65\ {\rm km\,s^{-1}}$ are separate features. Each have declining integrated flux densities and are less than zero after MJD 58000. This is an artefact of the removal of the spectral bandpass in the data-reduction process. This is an insignificant factor in the stronger features. This implies there are two new 6.7-GHz methanol periodic features ($+4.82$ and $+8.01\ {\rm km\,s^{-1}}$) and possibly a third ($+8.65\ {\rm km\,s^{-1}}$) reported here.

An ephemeris is created using the average of all the periodic features, both $\tau_{{\rm Int}_{6.7}}$ and $\tau_{{\rm Int}_{12.2}}$, but excluding those with statistically significant time lags (discussed in Section 5.2). Only the post-2003 observations are used to find the ephemeris because this data is more sensitive. For each of these features, the average of D_n (for $n = 8$–33) is determined and then using $\tau_{\rm Int} = 242$ d each is projected backwards to what its FC_8 would be. The mean ($D_{8_{ave}}$) and standard deviation is found for the entire sample. This and $\tau_{\rm Int}$ are used estimate the ephemeris:

$$D_n = (242 \pm 2) \times (n - 8) + (52955 \pm 18). \quad (2)$$

As in the case of equation (1), the error on the period is multiplicative. The limit of this ephemeris is reached when the projected error is equivalent to ± 121 d, or $n = -43$ and 59. Results are comparable to those produced by equation (1).

4.2 Results of velocity drifts

Via visual inspection of the 6.7- and 12.2-GHz methanol dynamic spectra there are obvious velocity variations. Some hint of this is present in Fig. 1. It is apparent in both that most features blueward of $v = +1.2\ {\rm km\,s^{-1}}$ are blue shifting and most redward are red shifting. The features are drifting away from each other, henceforth this variation is referred to as velocity drift. Estimations of visual drift, for 20 features (thirteen 6.7 and seven 12.2 GHz), is recorded in Table 3. Also, the results of linear regression fitting are shown in Table 3 for 26 v_{C_v} (fifteen 6.7 and eleven 12.2 GHz) features. Ten of the v_{C_v} features, five in both transitions, are presented in Fig. 8. It is notable, the close association for the 6.7- and 12.2-GHz methanol maser features.

It is difficult to determine individual feature velocity drifts for those between $v = +0.8$ and $+2.3\ {\rm km\,s^{-1}}$. Velocity drifts were confirmed in several features by fitting multiple Gaussian profiles, v_{G_v}, (12 6.7 GHz and 8 12.2 GHz) to selected epochs of observations, also shown in Table 3. For features where there is visual evidence, showing no confusion/line blending, and either of R_C^2 and R_G^2 has values greater than 50 per cent, a determination of velocity drift is presented in Table 3. Note that if a feature visually appears to have a constant velocity and either or both R_C^2 and R_G^2 <50 per cent then the feature's velocity is labelled constant (c). The velocity drift of thirteen features are uncertain owing to various issues including: multiple masers present, heavy line blending, and weakness of emission. Six are labelled constant, in particular, the strongest emission features at $v = +1.2\ {\rm km\,s^{-1}}$ for each transition. These two are comprised of many masers with significant line blending perhaps resulting in no or little velocity drift. Finally four features are red shifting (at $v > +1.2$ kms), while five are blue shifting (at $v < +1.2$ kms). The features in both transitions at $v \sim -3.0\ {\rm km\,s^{-1}}$ are recorded as blue shifting owing largely to visual inspection of the dynamical spectra. The goodness of fits are R_C^2 <50 per cent. However, the $v_{C_{12.2}} = -3.0\ {\rm km\,s^{-1}}$ may be comprised of two masers in Fig. 3(c) possibly making linear regression fitting problematic. There is weak or no detectable maser emission in the $v_{C_{6.7}} = -3.1\ {\rm km\,s^{-1}}$ feature before MJD 55000. This is reflected in the randomness in the velocities plotted in Fig. 8. Gaussian fitted values were better with R_G^2 values approaching 50 per cent and $M_{G_{6.7}} \sim M_{G_{12.2}}$. This, along with visual inspection, made the determination of blue shifting possible in each transition.

The new, and periodic, feature at $v_{C_{6.7}} = +4.82\ {\rm km\,s^{-1}}$ is also velocity drifting. This drift is even visible in Fig. 1. The results for $v_{C_{6.7}}$ and $v_{G_{6.7}}$ for this feature are plotted in Fig. 4. The velocity drift determined for the corrected flux density data and the Gaussian fitted data are similar, $M_{C_{6.7}} = +3.41 \pm 0.05 \times 10^{-5}$ versus $M_{G_{6.7}} = +2.87 \pm 0.05 \times 10^{-5}\ {\rm km\,s^{-1}\,d^{-1}}$. However, it is noted a periodicity in its $v_{G_{6.7}}$ time-series, 250 ± 19 d, it is within error of that determined

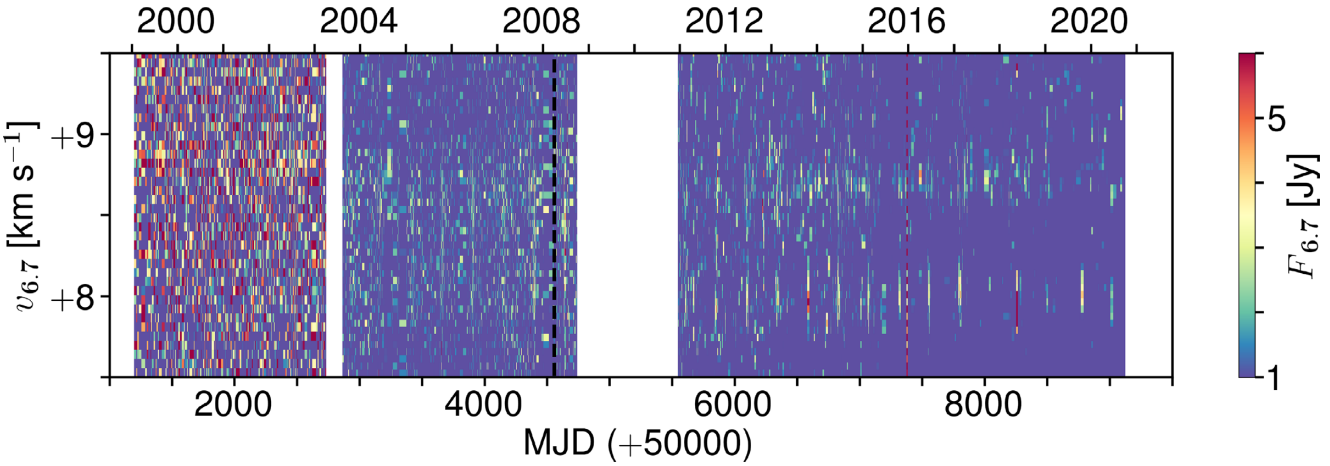

Figure 6. Dynamic spectra of the 6.7-GHz methanol masers in the velocity extent $v_{\mathrm{chan}_{6.7}} = +7.5$–$+9.5$ km s^{-1}. The black dashed vertical lines demarcate the date of the Sanna et al. (2015) interferometric observations.

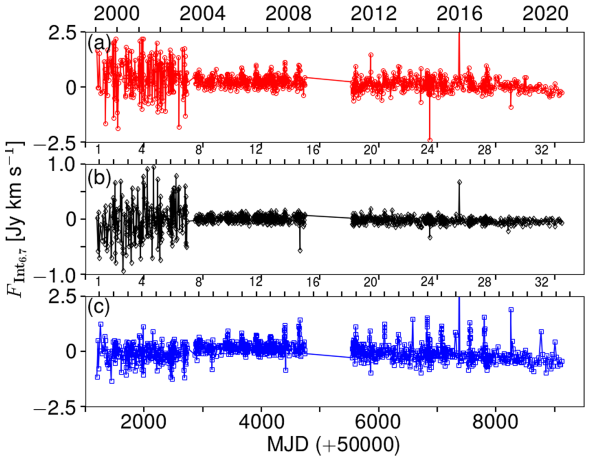

Figure 7. Time-series plots of the integrated flux density for emission (a) between $v_{\mathrm{Int}_{6.7}} = +8.38$ and $+8.91$ km s^{-1} (red circles), (b) between $v_{\mathrm{Int}_{6.7}} = +8.29$ and $+8.34$ km s^{-1} (black diamonds), and (c) between $v_{\mathrm{Int}_{6.7}} = +7.77$ and $+8.25$ km s^{-1} (blue squares).

for $F_{C_{6.7}}$ and $F_{G_{6.7}}$, 244 ± 6 d. This periodic nature of the velocity may be an artefact of the line blending with a non-periodic and non-drifting feature at $v_{6.7} = +5.3$ km s^{-1} and thus causing the difference between $\mathrm{M}_{C_{6.7}}$ and $\mathrm{M}_{G_{6.7}}$. Lastly, the maximum flux density of this feature $F_{C_{6.7}}$ is ∼1.5 times stronger than that of $F_{6.7}(v_{\mathrm{chan}} = +4.92)$. The flux density would have been reported decaying had the flux density not been corrected for the velocity drift.

In Table 3 only a single feature, at $v_{C_v} = +3.9$ km s^{-1}, had excellent goodness of fits for both its 6.7 and 12.2 GHz counterparts in each of their M_C and M_G values. This is a non-periodic feature. It is reported $M_{C_{6.7}} > M_{C_{12.2}}$ and $M_{G_{6.7}} > M_{G_{12.2}}$; both are red shifting. For comparison, another feature at $v_{C_v} = -0.27$ km s^{-1}, seen in both 6.7 and 12.2 GHz, had well fit velocity drifts for both the $v_{C_{6.7}}$ and $v_{G_{6.7}}$; each with excellent $R^2 \geq 90$ per cent. The velocity drifts determined from the fitted lines are $M_{C_{6.7}} = -3.22 \pm 0.03 \times 10^{-5}$ km s^{-1} d^{-1} and $M_{G_{6.7}} = -2.96 \pm 0.02 \times 10^{-5}$ km s^{-1} d^{-1}demonstrate the feature is blue shifting. However, no such good fit was determined for the 12.2-GHz emission. Thus it is unclear if it is drifting. The average line widths were different, $w_{G_{12.2}} = 0.40 \pm 0.03$ km s^{-1} versus $w_{G_{12.2}} = 0.29 \pm 0.02$. It is possible 12.2-GHz emission is comprised of more than one maser. It is noted that in Table 3 for all features with $w_{G_v} > 0.35$ km s^{-1} velocity drifts were marked as uncertain.

4.3 Summary of results

In a nutshell, the results are presented for the ongoing methanol maser monitoring observations of G9.62+0.20E, with data up to FC_{33}. Seven features have either become detectable after 2003, three 6.7 and two 12.2-GHz methanol masers, or weakened and/or become non-detectable, for the features $v_{6.7} \sim v_{12.2} \sim -2.0$ km s^{-1}, over the 21 yr of monitoring. New periodic features at $v_{C_{6.7}} = +4.82$, $+8.01$, and $+8.65$ km s^{-1} are identified. Some features in both the 6.7- and 12.2-GHz transitions drift in velocity contemporaneously. We report that there is a systematic velocity drift occurring; the maser features redward of $v = +1.2$ km s^{-1} are red shifting further while their blueward counterparts are blue shifting.

5 DISCUSSION

5.1 Historical results

Variability studies of 6.7- and 12.2-GHz methanol masers in a large sample of sources undertaken by Caswell et al. (1995a, b), respectively, act as excellent baseline observations to confirm earlier periodic flaring. Goedhart et al. (2003) showed the 6.7-GHz methanol masers of G9.62+0.20E varied by about 20 per cent between the quiescent, ∼4500 Jy, and maximum, ∼5500 Jy, phase. They found the 12.2 GHz masers rose from ∼150 Jy to ∼300 Jy, or a factor of two, during the flare cycle. Caswell et al. (1995b) reported no variability in the 6.7-GHz methanol masers of this source, $F_{6.7}$ ∼5090 Jy, but Caswell et al. (1995a) reported the 12.2-GHz counterparts varied from 130 Jy (observed between 1992 March 8−9), to a maximum of 180 Jy (observed on 1992 June 8), then back to 126 Jy (observed between 1992 December 22−23) over ∼290 d. We projected backwards the ephemerides determined from Goedhart et al. (2014) shown in equation (1) and here from equation (2) to estimate the maxima in which earlier FC_n would have occurred. The ephemerides have overlapping ranges for each FC_n. The historical observations are plotted in Fig. 9. It can be seen that the Caswell et al. (1995a) data peak in the error range of FC_{-9} on 1992 June 29 (±20 d) for the Goedhart et al. (2014) ephemeris but was at the error

Table 3. Linear regression analysis of velocity drifts for both corrected and Gaussian-fitted velocities for selected 6.7- and 12.2-GHz methanol maser features in the dynamic spectra. The slope, intercept, and determination of goodness of fit, R^2, are given for selected features; the reported errors in parenthesis are on the last digit. Errors presented in parenthesis for the period are a measure of standard deviation.

Trans.	Corrected velocity[a]				Gaussian-fitted velocity[b]					Velocity Drift	
	v_C	Slope, M_C ($\times10^{-5}$	Intercept	R^2_C	v_G	w^c_G FWHM	Slope, M_G ($\times10^{-5}$)	Intercept	R^2_G	Vis.	
(GHz)	(km s^{-1})	(km s^{-1} d^{-1})	(km s^{-1})	(%)	(km s^{-1})	(km s^{-1})	(km s^{-1} d^{-1})	(km s^{-1})	(%)	Insp.[d]	Drift[e]
6.7	+8.2(2)	−0.6(4)	+8.19(3)	0		Insufficient epochs detected and or fitted				u	u
12.2	+8.3(1)	−0.1(4)	+8.35(2)	0		Insufficient epochs detected and or fitted				u	u
6.7	+6.39(3)	+0.83(5)	+6.345(3)	25	+6.41(2)	0.19(3)	+0.84(3)	+6.351(2)	62	c	r
6.7	+5.29(2)	+0.01(4)	+5.284(2)	0	+5.30(1)	0.39(4)	+0.10(3)	+5.290(2)	3	c	c
12.2	+5.6(3)	+0.4(6)	+5.59(3)	0		Insufficient epochs detected and or fitted				u	u
6.7	+4.82(7)	+3.38(5)	+4.638(3)	82	+4.84(6)	0.23(4)	+2.87(5)	+4.650(3)	91	r	r
6.7	+3.9(1)	+5.99(6)	+3.570(3)	92	+4.0(1)	0.30(7)	+5.83(6)	+3.573(4)	97	r	r
12.2	+3.9(1)	+5.45(6)	+3.578(3)	91	+3.97(7)	0.30(4)	+4.94(9)	+3.615(7)	93	r	r
6.7	+3.14(4)	+1.00(7)	+3.088(4)	16	+3.13(6)	0.39(6)	+1.1(2)	+3.06(1)	11	r	u
12.2	+3.16(7)	−0.6(1)	+3.190(8)	2	+3.15(7)	0.3(3)	−5.5(4)	+2.73(3)	46	r	u
6.7	+2.31(5)	+1.82(6)	+2.210(4)	45	+2.3(1)	0.5(1)	+6.0(2)	+1.90(1)	70	r	u
12.2	+2.16(8)	+2.3(1)	+2.044(8)	22	+2.19(8)	0.4(2)	+1.4(6)	+2.08(5)	3	r	u
6.7					+1.71(8)	0.5(2)	+3.5(1)	+1.481(8)	72	u	u[f]
12.2					+1.52(4)	0.44(4)	−0.7(2)	+1.57(1)	7	u	u[f]
6.7	+1.21(2)	+0.46(3)	+1.188(2)	16	+1.21(1)	0.32(1)	+0.41(2)	+1.186(1)	62	c	c[f]
12.2	+1.250(3)	+0.00(2)	+1.250(1)	0	+1.254(9)	0.22(1)	+0.35(4)	+1.229(3)	29	c	c[f]
6.7	+0.74(5)									u	u[f]
12.2	+0.76(5)									u	u[f]
6.7	+0.33(6)	−0.6(1)	+0.361(6)	3	+0.31(3)	0.25(4)	−0.94(4)	+0.372(3)	82	b	b
6.7	−0.27(6)	−3.18(3)	−0.099(2)	92	−0.28(6)	0.29(2)	−2.96(2)	−0.087(2)	98	b	b
12.2	−0.26(5)	−1.92(8)	−0.161(4)	42	−0.29(2)	0.40(3)	−0.75(9)	−0.238(7)	23	u	u
6.7	−0.90(3)	−1.53(3)	−0.816(2)	74	−0.90(3)	0.32(4)	−1.24(3)	−0.817(2)	84	b	b
12.2	−1.01(2)	+0.39(5)	−1.026(3)	7	−0.99(1)	0.34(4)	−0.21(5)	−0.975(4)	7	c	c
6.7	−1.18(6)	+2.23(9)	−1.302(5)	39		Insufficient epochs detected and or fitted				b	u
6.7	−1.95(5)	+0.10(8)	−1.956(6)	0		Insufficient epochs detected and or fitted				c	c
12.2	−2.0(1)	+1.0(2)	−2.05(1)	3		Insufficient epochs detected and or fitted				c	c
6.7	−3.1(2)	−5.1(3)	−2.79(2)	20	−3.17(7)	0.29(9)	−4.8(3)	−2.80(2)	49	b	b
12.2	−3.0(3)	+0.0(5)	−2.40(3)	38	−3.15(7)	0.3(3)	−5.5(4)	−2.73(3)	46	b	b

[a]Linear regression fitting to the associated velocities of corrected flux densities.
[b]Linear regression fitting to the associated velocities of Gaussian-fitted velocities in selected spectra.
[c]Full width at half-maximum line width, w_{G_v}.
[d]Visual inspection of velocity drifts: blueward (b) or redward (r), constant (c) or uncertain (u).
[e]Determination of velocity drifts: blueward (b) or redward (r), constant (c) or uncertain (u).
[f]Results of regression fitting are inconclusive in velocity ranges with significant line blending, e.g. $v_v = +0.8$ to $+2.3$ km s^{-1}.

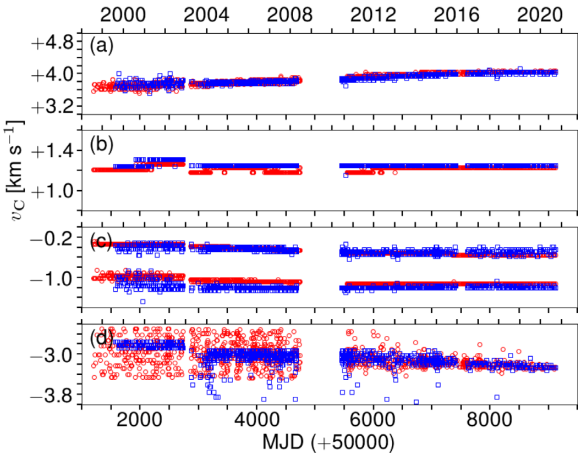

Figure 8. Time-series plots of the velocities v_{C_v} associated with the maximum flux density in each epoch F_{C_v} in the velocity range (a) $v_{\mathrm{chan}_v} = +3.0$–$+5.0$ km s^{-1}, (b) $v_{\mathrm{chan}_v} = +0.8$–$+1.6$ km s^{-1}, (c) $v_{\mathrm{chan}} = -1.4$–$+0.2$ km s^{-1}, and (d) $v_{\mathrm{chan}_v} = -4.0$–$-2.4$ km s^{-1}. The 6.7- and 12.2-GHz velocities are represented by red circles and blue squares, respectively.

limit of the ephemeris from equation (2). A new review of the 6.7-GHz observations presented in Caswell et al. (1995b) may identify evidence of contemporaneous flaring with the 12.2-GHz masers.

Historical observations prior to 1999 were also taken at HartRAO towards G9.62+0.20E. Regrettably, the data were lost when the original control computer failed, however, time-series of various velocity channels at both 6.7 and 12.2 GHz were saved; these are shown in Fig. 9. We see evidence of flaring during FC_{-7}. It appears the peak of FC_{-9} is found between when $F_{12.2}$ reaches its maximum in Caswell et al. (1995b) and that for the $F_{6.7}$ HartRAO observations. Also the ephemeris from equation (2) suggests HartRAO observations missed the maximum in both 6.7 and 12.2 GHz. Fig. 9 serves to demonstrate (1) this was possibly periodic at least as early as 1992 and (2) data mining may identify candidate periodic sources.

5.2 Time lags

The periodic flaring nature of the methanol masers lend themselves to measuring time lags and possibly measuring distances between features. Goedhart et al. (2014) measured time lags in G9.62+0.20E ranging from a few days to 34 d; the largest was between $v_{\mathrm{chan}_{6.7}} =$

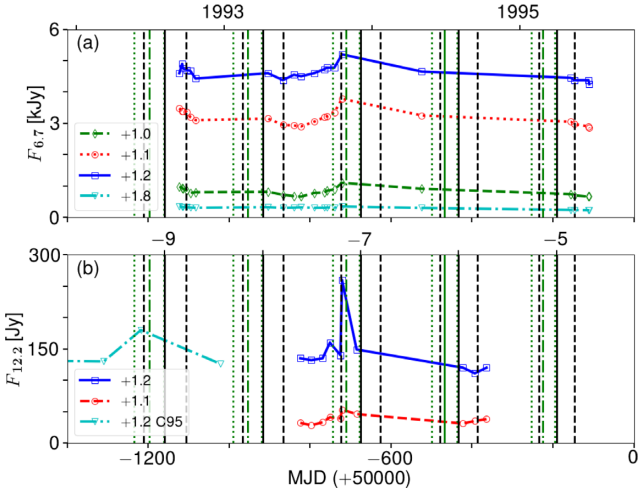

Figure 9. Time-series plots of (a) 6.7- and (b) 12.2-GHz methanol maser velocity channels associated with G9.62+0.20E. The velocity channels plotted are listed in each. The $F_{12.2}$ results from Caswell et al. (1995b) (C95; green dot-dashed line) are plotted. Vertical lines demarcate the predicted FC_n from ephemerides shown in equation (2) (black solid and minimum & maximum in dashed lines) and equation (1) (Goedhart et al. 2014) (green solid and minimum & maximum in dotted lines).

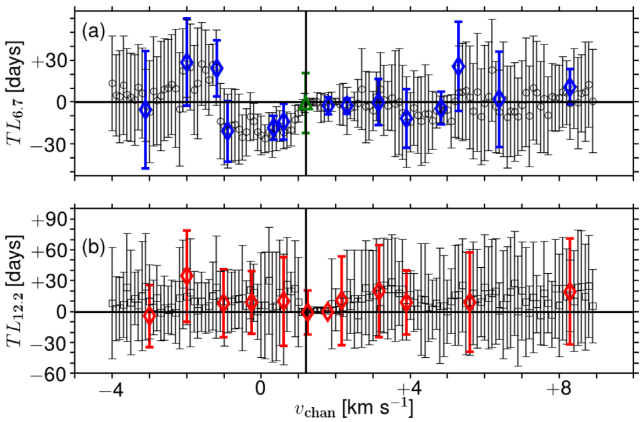

Figure 10. Velocity versus time lags estimated from the difference between the brightest feature ($v_{6.7} = +1.2$ km s^{-1}) and selected $v_{\rm chan_\nu}$ associated with G9.62+0.20E are plotted. The values of individual maser velocities (a) $v_{\rm chan_{6.7}}$ and (b) $v_{\rm chan_{12.2}}$ are represented in black circles and squares, respectively. Values for features identified in Table 3 are plotted as bold blue diamonds (6.7 GHz) and bold red diamonds (12.2 GHz). All error bars represent 1σ standard deviation measures. The bold green triangle represents the time lag between the brightest features in 6.7 and 12.2 GHz.

-0.222 km s^{-1} that lagged $v_{\rm chan_{6.7}} = +1.227$ km s^{-1}. The statistical analysis described here is used to estimate these lags to confirm those in Goedhart et al. (2014) and estimate errors (1σ).

Time lags were measured for emission in every $v_{\rm chan_\nu}$ from -4.0 to $+9.0$ km s^{-1} in both transitions in comparison to emission in $v_{\rm chan_{6.7}} = +1.22$ km s^{-1} and plotted in Fig. 10. No time lags for any $v_{\rm chan_{12.2}}$ are statistically significant but are for those found for $-0.5 \leq v_{\rm chan_{6.7}} \leq +0.9$ km s^{-1} 6.7-GHz emission. Time-series plots of $F_{\rm Int_{6.7}}$ for $v_{6.7} = +1.22 \pm 0.04$ and $+0.7 \pm 0.2$ km s^{-1}, during FC_{25} to FC_{27}, are shown in Fig. 11. A time lag is visible. Hence, time lags were estimated for all features listed in Table 2, compared to $F_{\rm Int_{6.7}}$ for $v_{6.7} = +1.22 \pm 0.04$ km s^{-1}, and only four ($v_{Int_{6.7}} = -1.18$, -0.31, $+0.39$, and $+0.72$ km s^{-1}) are statistically meaningful. The feature,

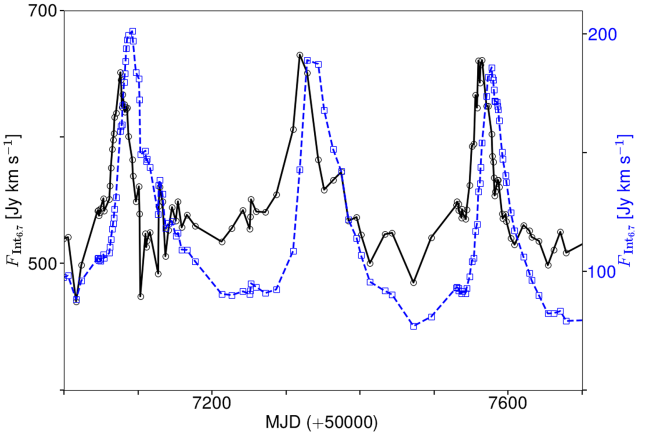

Figure 11. Time-series plots of the integrated flux density of selected features at $v_{\rm Int_{6.7}} = +1.2$ km s^{-1} (solid black line with circles) plotted against the primary y-axis and the $v_{\rm Int_{6.7}} = +0.7$ km s^{-1} (dashed blue line with squares) plotted against the secondary y-axis.

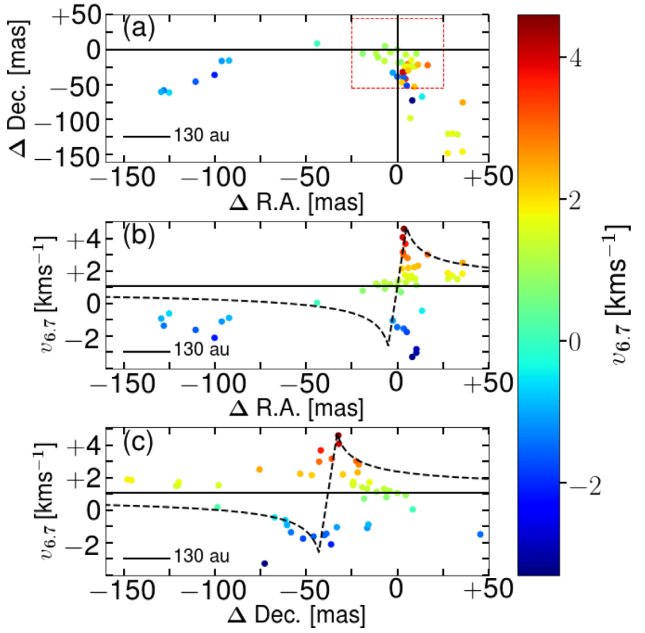

Figure 12. Panel (a): spot map of 6.7-GHz methanol masers associated with G9.62+0.20E. The red dashed rectangle represents the region in which periodic features may reside. Position–velocity plots: (panel b) right ascension and (panel c) declination offsets versus feature velocities. A simple Keplerian rotation model (bold dashed black lines) is included. The solid black line demarcates $v_{\rm lsr} = +1.05$ km s^{-1}, the velocity of the brightest 6.7-GHz methanol maser.

$v_{\rm Int_{6.7}} = -1.18$ km s^{-1}, with the largest lag ($+24 \pm 20$) is determined to be non-periodic ergo the time lag is meaningless. This leaves only three features, $v_{\rm Int_{6.7}} = -0.31$, $+0.39$, and $+0.72$ km s^{-1}, which are periodic and have $\mathrm{Tl}_{Int_{6.7}} = -13$, -19, and -14 d respectively. Two have a 12.2 GHz counterpart that is not periodic while the other has no 12.2-GHz emission.

The statistically significant time lags are $\sim -15 \pm 10$ d. At the speed of light, these lags imply the individual maser features are separated by $\sim 2600 \pm 1700$ au. The 6.7-GHz maser spot map, data taken from Sanna et al. (2015) is plotted in Fig. 12. In this plot the region demarcated by the rectangle was proposed by Sanna

et al. (2015) to contain the periodic masers. If the masers are all in close proximity to the plane of the sky, then they are separated by ∼300 au and the estimated propagation rate is anywhere from ∼10 to 35 per cent the speed of light. Burns et al. (2020) reported methanol masers associated with G358.93 − 0.03 were activated when a major accretion event caused a heat wave moving outward at ∼4 per cent light speed. Cepheus A also had measured time lags and Szymczak, Wolak & Bartkiewicz (2014) suggested these were the result of position and light traveltime. The time lags may simply be an artefact of the differences in the conditions of the maser cloudlets. Cragg, Sobolev & Godfrey (2005) proposed that Class II methanol masers, such as 6.7- and 12.2-GHz transitions, will activate and saturate differently under a range of conditions possibly accounting for these time lags. It is noted that the features with time lags range from modest (60 and 200 Jy) to bright (2000 Jy) maser sources. Conversely, if the disturbance does propagate at the speed of light then the masers may reside in a disc seen nearly 'edge-on' and separated by a vector from 4° ($TL \sim 25$ d) to 19° ($TL \sim 5$ d) (see more discussion in Section 5.3).

In the spot map shown in Fig. 12, it is clear many maser features with similar velocities reside in different regions. This fact may explain why features at $v_{C_{12.2}} = -0.26$ and $+0.76$ km s^{-1} have no measurable time lags. Though it is estimated where the periodic masers reside, a more thorough investigation is required with very long baseline interferometry to identify where each is.

5.3 Maser velocity drifts

Water masers undergo significant velocity drifts. For example, Lekht, Mendoza-Torres & Sorochenko (1995) reported a water maser feature associated with W75S red shifted 1 km s^{-1} over 3.5 yr, or $M_{22.2} \sim 8 \times 10^{-4}$ km s^{-1} d^{-1}. They proposed this variation is the result of shocks resulting from increased wind activity. Velocity drifts are also reported in methanol masers. Szymczak et al. (2014) found several maser features associated with Cepheus A demonstrating velocity drifts of between $M_{6.7} \sim 1{-}3 \times 10^{-4}$ km s^{-1} d^{-1}; some features blue shifted and others red shifted. They suggested some of these features were comprised of multiple masers. Szymczak et al. (2015) also reported velocity variation in a single 6.7 GHz CH_3OH feature associated with G22.357 + 0.066; the feature survived ∼520 d and experienced a rate of velocity drift of 0.24 km s^{-1} yr^{-1}, or $M_{6.7} \sim 6.5 \times 10^{-4}$ km s^{-1} d^{-1}. They are not certain if this is the result of heavily blended maser features or by the motion of the gas. Szymczak et al. (2018a) found several more sources with velocity drifts; again they suggest these are the result of variations of close or line-blended features but some may identify infalling gas.

Here, several features are presented experiencing systematic velocity drifts, and over many years, made obvious in Fig. 2 (6.7 GHz) and 3 (12.2 GHz) and listed in Table 3. Six were found to be constant over the over 20 yr of observation. In total, 13 could not be determined to be drifting or even constant mostly the result of significant line blending, in line with that proposed by Szymczak et al. (2018a). The remaining where the velocity drift is determined are simpler maser features predominantly comprised of a single maser. These remaining features demonstrate a systematic velocity drift about $v = +1.2$ km s^{-1} and is confirmed by (1) seen in both transitions and at similar values for features with similar velocities and (2) Gaussian-fitted results confirm drifts in each feature. The similarity of velocity drifts for each transition supports the argument put forward by Sanna et al. (2015) stating these features in each transition co-exist in the same maser cloudlets.

There are many explanations for this systematic velocity drifting. For example, variations of heavily line blended masers in a feature create the appearance of velocity variation (Szymczak et al. 2018a). There certainly is evidence of low-gain masers, as one notes the striations at each flare maximum in Fig. 2. Sanna et al. (2015) stated there may be more low gain masers that were resolved out of their observations. However, it is statistically difficult for such flux density variations to cause systematic velocity drifts. Turbulence, shocks, and/or outflows will cause velocity variations and perhaps in a systematic way. However, flux density variations do not seem to support this explanation; features are present for tens of years and have slowly varying quiescent phases.

Both features experiencing the largest drift, $v_{C_v} = -3.0$ and $+3.9$ km s^{-1}, appear to lie in close proximity shown in Fig. 12, about ∼40 mas (∼185 au at 4.7 kpc) south of the brightest features in 6.7- and 12.2-GHz methanol (seen at ΔRA = ΔDec. = 0 mas). A simple solution might be a rotating Keplerian disc. This hypothesis can be tested by plotting the position–velocity diagrams from the maser spots found in Sanna et al. (2015), see included in Fig. 12 for the 6.7-GHz masers. Seifried et al. (2016) model PV diagrams for discs that vary in inclination from 'face-on', inclination angle (with respect to the line of sight) $i = 0°$, to 'edge-on', $i = 90°$. They find that a recognizable Keplerian rotation profile is visible for 'edge-on' discs and up to ∼30° of a 'face-on' disc. A similar rotation profile is visible in Fig. 12. The velocity centre is shifted to $v_{6.7} = +1.05$ km s^{-1}, the velocity of the brightest 6.7-GHz methanol maser feature, and the position centre is moved by 38 mas for the declination plot. Three aspects of the PV diagram representing the clearest indication of the Keplerian model are used to determine the best-fitting parameters: (1) the maximum velocity feature $v_{6.7} = +4.8$ km s^{-1}, (2) the features at $v_{6.7} = +3.0$ and 2.5 km s^{-1}, and (3) those features with $+1.05 \leq v_{6.7} \leq +4.8$ km s^{-1}. If we use the central mass $M_\star = 12\,M_\odot$ (∼B1 star) (Hofner et al. 1996) and assume radii $R_{\rm inner} = 5$ au and $R_{\rm outer} = 5000$ au the best fit is achieved with an inclination angle of 22°. It is important to note that the best-fitting results are depend upon the sensitivity achieved in the observations made to create the maser spot map. The inclination angle is similar to that in Sanna et al. (2015); they suggested it is ∼25°. Both are larger than that estimated to explain the time lags measured here. Perhaps the structure shown in Sanna et al. (2015) is a sub-structure of a larger disc proposed here; its velocity gradient is ∼0.5 km s^{-1} whereas here it is ∼8 km s^{-1}. High sensitivity/resolution, multiple-epoch, and interferometric observations are required to resolve this. A wide range of solutions can be produced from the limited constraints here but it is gratifying that the simple Keplerian model using published results can fit well the PV plot in Fig. 12.

From the simple Keplerian model, fitted to the results in Fig. 13, we can estimate the necessary variations of each parameter to explain our systematic velocity drifts. We first estimate the typical velocity drift seen here, $M \sim 0.2$ km s^{-1} over the 7300 d of monitoring. In terms of mass accretion, we would require a growth in mass of ∼1 $M_\odot$ or ∼0.05 $M_\odot$ yr^{-1}. The extraordinary accretion event that occurred in S255IR-NIRS 3 was the result of an accretion rate $m_{\rm acc} = 5 \times 10^{-3}\,M_\odot$ yr^{-1} (Caratti o Garatti et al. 2017). This is an order of magnitude smaller than that required here, and to occur yearly for 20 yr, to explain the velocity drift. For a precessing disc, we estimate the variation in inclination angle is 1.°33 over this period. This implies the disc would complete one precession cycle in ∼5400 yr. Lastly, if the inner radius, $R_{\rm inner}$, decreases by 0.38 au or 0.073 mas over 20 yr, we can account for this velocity drift. Szymczak et al. (2018a) suggested infall is occurring in other sources. It is possible velocity drifting masers in Cepheus A (Szymczak et al. 2014) experienced a

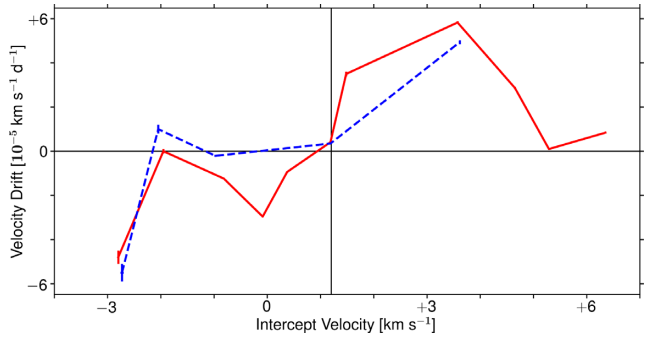

Figure 13. Plots of velocity drifts versus the fitted intercept velocities for 6.7 (red) and 12.2 GHz (blue) maser features associated with G9.62+0.20E.

trend similar to that shown in Fig. 13, regrettably too few features had measurable velocity drifts (only four). It is possible that either, or a combination of both, a precessing disc or infalling gas explain the velocity drifts seen here but it will be very difficult to prove. Only multi-epoch high spatial resolution interferometric observations can determine the veracity of our hypothesis.

6 SUMMARY AND FUTURE WORK

Presented here are simple tools useful in studying maser variations seen in dynamic spectra. The results from these tools are confirmed by (1) the similarity between transitions and (2) in comparison to Gaussian-fitted results. A new periodically varying 6.7-GHz methanol maser feature associated with G9.62+0.20E at $v_{C_{6.7}} = +4.82$ km s^{-1} is reported and two weak periodic features at $v_{Int_{6.7}} = +8.01$ and $+8.65$ km s^{-1}. Evidence of periodic flaring as early as 1992 is seen in historical data. The ephemeris produced here is within errors of that determined from Goedhart et al. (2014). Statistically significant time lags are confirmed but it is not clear what is their cause. Nine features are experiencing velocity drifts and many have contemporaneously varying 6.7- and 12.2-GHz maser velocities. Most amazing, they appear to drift systematically about the brightest maser feature, $v = +1.2$ km s^{-1}. The red shifted features are becoming more red while the blue shifting ones are becoming more blue. It is proposed a best-fitting rotating Keplerian disc with a central mass of $\sim$12 M$_\odot$, radii $R_{\rm inner} = 5$ au and $R_{\rm outer} = 5000$ au, and at an inclination angle of 22° either precessing and/or experiencing infall explains these systematic velocity drifts.

New multi-epoch interferometric observations and continuing monitoring are required to first determine the exact positions of the periodically varying features and secondly explain the cause of these systemic velocity drifts.

ACKNOWLEDGEMENTS

We thank Dr. Jonathan Quick for his tireless effort to ensure the monitoring of observing programmes continue at HartRAO. We would also like to thank the Maser Monitoring Organisation (M2O) for support. Specifically, our appreciation to Dr. Yoshinori Yonekura and Dr. Marian Szymczak for sharing their maser monitoring data to help our effort in confirming velocity drifts in this paper. We thank an anonymous referee for comments leading to the improvement of this manuscript. The Hartebeesthoek 26-m telescope is operated by the South African Radio Astronomy Observatory, which is a facility of the National Research Foundation, an agency of the Department of Science and Innovation.

DATA AVAILABILITY

The data underlying this paper were accessed from Hartebeesthoek Radio Astronomy Observatory. Public domain access is being developed but not yet available. The derived data generated in this research will be shared on a reasonable request to G. MacLeod. The Long Baseline Array (LBA) data are published in Sanna et al. (2015). Raw data from the LBA are made available through the Australia Telescope Online Archive (ATOA) and through search forms on the CSIRO Data Access Portal.

REFERENCES

Araya E. D., Hofner P., Goss W. M., Kurtz S., Richards A. M. S., Linz H., Olmi L., Sewiło M., 2010, ApJ, 717, L133
Burns R. A. et al., 2020, Nat. Astron., 4, 506
Caratti o Garatti A. et al., 2017, Nat. Phys., 13, 276
Caswell J. L., Vaile R. A., Ellingsen S. P., Norris R. P., 1995a, MNRAS, 274, 1126
Caswell J. L., Vaile R. A., Ellingsen S. P., Whiteoak J. B., Norris R. P., 1995b, MNRAS, 272, 96
Cragg D. M., Sobolev A. M., Godfrey P. D., 2005, MNRAS, 360, 533
Felli M. et al., 2007, A&A, 476, 373
Fujisawa K. et al., 2014, PASJ, 66, 78
Garay G., Rodriguez L. F., Moran J. M., Churchwell E., 1993, ApJ, 418, 368
Gaylard M. J., 2010, MNASSA, 69, 168
Goedhart S., Gaylard M. J., van der Walt D. J., 2003, MNRAS, 339, L33
Goedhart S., Gaylard M. J., van der Walt D. J., 2004, MNRAS, 355, 553
Goedhart S., Langa M. C., Gaylard M. J., Van Der Walt D. J., 2009, MNRAS, 398, 995
Goedhart S., Maswanganye J. P., Gaylard M. J., van der Walt D. J., 2014, MNRAS, 437, 1808
Goedhart S., van Rooyen R., van der Walt D. J., Maswanganye J. P., Sanna A., MacLeod G. C., van den Heever S. P., 2019, MNRAS, 485, 4676
Green J. A., Caswell J. L., Voronkov M. A., McClure-Griffiths N. M., 2012, MNRAS, 425, 1504
Hofner P., Kurtz S., Churchwell E., Walmsley C. M., Cesaroni R., 1996, ApJ, 460, 359
Inayoshi K., Sugiyama K., Hosokawa T., Motogi K., Tanaka K. E. I., 2013, ApJ, 769, L20
Lekht E. E., Mendoza-Torres E., Sorochenko R. L., 1995, ApJ, 443, 222
MacLeod G. C., Gaylard M. J., 1996, MNRAS, 280, 868
MacLeod G. C. et al., 2018, MNRAS, 478, 1077
Maswanganye J. P., Gaylard M. J., Goedhart S., Walt D. J. v. d., Booth R. S., 2015, MNRAS, 446, 2730
Maswanganye J. P., van der Walt D. J., Goedhart S., Gaylard M. J., 2016, MNRAS, 456, 4335
Moscadelli L. et al., 2017, A&A, 600, L8
Olech M., Szymczak M., Wolak P., Gérard E., Bartkiewicz A., 2020, A&A, 634, A41
Ott M., Witzel A., Quirrenbach A., Krichbaum T. P., Standke K. J., Schalinski C. J., Hummel C. A., 1994, A&A, 284, 331
Parfenov S. Y., Sobolev A. M., 2014, MNRAS, 444, 620
Proven-Adzri E., MacLeod G. C., Heever S. P. v. d., Hoare M. G., Kuditcher A., Goedhart S., 2019, MNRAS, 487, 2407
Sanna A., Reid M. J., Moscadelli L., Dame T. M., Menten K. M., Brunthaler A., Zheng X. W., Xu Y., 2009, ApJ, 706, 464
Sanna A. et al., 2015, ApJ, 804, L2
Sanna A., Moscadelli L., Surcis G., van Langevelde H. J., Torstensson K. J. E., Sobolev A. M., 2017, A&A, 603, A94
Scargle J. D., 1982, ApJ, 263, 835
Seifried D., Sánchez-Monge Á., Walch S., Banerjee R., 2016, MNRAS, 459, 1892
Sugiyama K. et al., 2015, Publ. Korean Astron. Soc., 30, 129
Sugiyama K. et al., 2017, PASJ, 69, 59
Szymczak M., Wolak P., Bartkiewicz A., van Langevelde H. J., 2011, A&A, 531, L3

Szymczak M., Wolak P., Bartkiewicz A., 2014, MNRAS, 439, 407
Szymczak M., Wolak P., Bartkiewicz A., 2015, MNRAS, 448, 2284
Szymczak M., Olech M., Wolak P., Bartkiewicz A., Gawroński M., 2016, MNRAS, 459, L56
Szymczak M., Olech M., Sarniak R., Wolak P., Bartkiewicz A., 2018a, MNRAS, 474, 219
Szymczak M., Olech M., Wolak P., Gérard E., Bartkiewicz A., 2018b, A&A, 617, A80
van den Heever S. P., van der Walt D. J., Pittard J. M., Hoare M. G., 2019, MNRAS, 485, 2759
van der Walt D. J., Goedhart S., Gaylard M. J., 2009, MNRAS, 398, 961
van der Walt D. J., Maswanganye J. P., Etoka S., Goedhart S., van den Heever S. P., 2016, A&A, 588, A47
Weaver H., Dieter N. H., Williams D. R. W., 1968, ApJS, 16, 219

This paper has been typeset from a TEX/LATEX file prepared by the author.